

# The Mass distribution of the Most Luminous X-ray Cluster RXJ1347.5-1145 from Gravitational Lensing

Philippe Fischer<sup>1,2</sup>

Dept. of Astronomy, University of Michigan, Ann Arbor, MI 48109

J. Anthony Tyson

Bell Laboratories-Lucent Technologies, 700 Mountain Ave., Murray Hill, NJ 07974

## ABSTRACT

Galaxy cluster mass distribution are potentially useful probes of  $\Omega_0$  and the nature of the dark matter. Large clusters will distort the observed shapes of background galaxies through gravitational lensing allowing the measurement of the cluster mass distributions. In this paper we describe weak statistical lensing measurements of the most luminous X-ray cluster known, RXJ1347.5-1145 at  $z = 0.45$ . We detect a shear signal in the background galaxies at a signal-to-noise ratio of 7.5 in the radial range  $120 \leq r \leq 1360h^{-1}$  kpc. A mass map of the cluster reveals an  $11\sigma$  peak in the cluster mass distribution consistent with the position of the central dominant galaxy and  $3\sigma$  evidence for the presence of a subcluster at a projected radius of  $1.3 - 1.7 h^{-1}$  Mpc from the cluster center. In the range  $120 \leq r \leq 1360h^{-1}$  kpc mass traces light, and the azimuthally averaged cluster mass and light profiles are consistent with singular isothermal spheres with  $M(r < 1 \text{ Mpc}) = 1.7 \pm 0.4 \times 10^{15} M_\odot$ . Assuming an isotropic velocity distribution function, the implied velocity dispersion is  $\sigma = 1500 \pm 160 \text{ km s}^{-1}$ . The rest-frame mass-to-light ratio is  $M/L_B = 200 \pm 50h M_\odot/L_{B\odot}$ . The lensing mass estimate is almost twice as high as a previously determined X-ray mass estimate.

## 1. Introduction

Galaxy clusters are useful probes of large scale structure, and their mass distributions reflect the underlying cosmology (Richstone et al. 1992). Specific predictions are emerging from large scale structure simulations regarding the mass distributions in clusters, the degree of sub-clustering, and the relationship between light and mass and how these vary when cosmological parameters ( $\Omega$ , slope of the density perturbation spectrum, type of dark matter particles, etc) are varied. Accurate surface mass density measurements for a sample of clusters can thus place strong constraints on  $\Omega$  and the nature of the dark matter (Crone et al. 1994, Crone et al. 1996, Wilson et al 1996). Cluster mass measurements are also useful tests of big bang nucleosynthesis; coupled with gas and stellar mass estimates, the ratio of baryonic matter to dark matter,  $\Omega_B$ , can be estimated (White & Fabian 1995, Evrard 1997).

The relative numbers of massive clusters found at redshifts  $z = 0.2$  and  $z = 0.5$  is a sensitive test of  $\Omega$ . In this redshift range rich clusters evolve in mass much more rapidly in high  $\Omega$  universes; at  $z = 0.5$  seven times as many massive clusters are expected for  $\Omega = 0.3$  than for  $\Omega = 1$ , while at  $z = 0.2$  about four times as many massive clusters are expected for  $\Omega = 1$  than for  $\Omega = 0.3$ ,

---

<sup>1</sup>Visiting Astronomer, National Optical Astronomy Observatories, which is operated by the Association of Universities for Research in Astronomy, Inc., under contract to the National Science Foundation.

<sup>2</sup>Hubble Fellow

independent of  $\Lambda$  (Eke et al 1996). So it is important to measure the masses of clusters at  $z = 0.5$  as well as  $z = 0.2$ .

The study of the mass distributions in galaxy clusters via gravitational lensing is now a well established technique (Tyson et al 1990, Tyson & Fischer 1995, Squires et. al. 1996a, 1996b, 1996c and Fischer et al. 1996). Lensing provides the only direct means of measuring cluster masses; unlike dynamical and X-ray mass estimates it does not depend on knowledge of the dynamical state of the matter.

The cluster RXJ 1347.5-1145, at a redshift of  $z = 0.451$ , is the most luminous X-ray cluster known with a bolometric luminosity  $L_X = 2 \times 10^{46}$  erg  $s^{-1}$  (Schindler et al. 1995). As reported by Schindler et al. (1995) there are two arc candidates at projected angular distances of around  $35''$  ( $120 h^{-1}$  kpc) from the central dominant galaxy (CDG), which implies a large amount of mass contained within that radius. However, the X-ray mass estimate (Schindler et al. 1996) is much lower than implied by the arcs, and is also lower than would be naively expected from the total X-ray luminosity.

We have obtained deep optical CCD images of RXJ1347.5-1145 in two bandpasses over a wide field in order to study the cluster mass distribution by its distorting effect on the shapes of background galaxies. These observations are described in §2. In §3 we discuss the galaxy photometry and shape analysis. §4 describes the technique used to correct for PSF anisotropy. §5 shows the radial shear profile of the cluster and §6 describes the equations for one and two-dimensional mass reconstruction. §6.2 contains a description of simulations carried out to quantify the dilution due to seeing and §6 is a discussion of the cluster mass distribution, total mass and mass-to-light ratio. §6 also has a comparison of the X-ray mass estimate and the lensing mass estimate.

## 2. Observations

The cluster RXJ1347-1145 was observed using the prime focus CCD camera on the Blanco 4m at CTIO on 26 June 1995. The total exposure time was 4800s in  $B_J$  ( $16 \times 300$ s) and 3300s in R ( $11 \times 300$ s). The telescope was dithered between exposures. The “Tek4” 2048<sup>2</sup> thinned SITE CCD was used with  $0.43''$  pixels. The seeing on the combined  $B_J$  image averaged  $1.2''$  FWHM and  $1.25''$  for the combined R image, but was variable across the images (see §4). The night was not photometric so the images were normalized prior to combining. Additional images were obtained on the two previous nights, however, due to poor image quality ( $\approx 2''$  FWHM), they were not used. The total useable field size in the combined images is approximately  $14.3' \times 14.0'$  for  $B_J$  and  $14.5' \times 14.2'$  for R. The RMS sky noise is 29.1  $B_J$  mag per square arcsec and 27.7 R mag per square arcsec. A color image of a subsection of the the CCD field centered on the cluster is shown in Fig. 1.

Fig. 1.— Color image of the RXJ1347.5-1145 field constructed from  $B_J$  and R band images. This extract of our larger CCD field measures 6.8 arcminutes on a side. The log of the intensity is shown. North is up and East is to the left.

### 3. Faint Galaxy Photometry and Analysis

The faint galaxy analysis was carried out using the analysis software ProFit (developed by PF). This software, starting with the brightest objects, fits an analytical model to each, using weighted, non-linear least squares, and subtracts the light from the image. It then proceeds to successively fainter objects. Once it has detected and subtracted all the objects in an image it replaces each in turn and refits and resubtracts until convergence is achieved. The software outputs brightness, orientation, ellipticity and other image parameters based on the fitted function.

Fig. 2 shows  $B_J$  galaxy counts for the faint galaxies in the field of RXJ 1347-1145. The magnitudes are isophotal magnitudes with outer isophote of 28.9  $B_J$  mag square arcsecond (30.8  $B_J$  mag per pixel).

The lower panel of Fig. 3 shows a  $B_J$ -R color magnitude diagram of the whole field. There are a large number of red galaxies with an indication of a gap around  $B_J - R = 1.6$  mag. The upper panel shows only the inner 90'' and one can now clearly see the cluster early-type galaxy sequence centered around  $B_J - R = 2.3$  mag.

### 4. PSF Anisotropy

There are several factors which can contribute to PSF anisotropy (Kaiser et al 1995). In June 1995 at the CTIO 4m there were at least two known contributors, telescope astigmatism (and possible misalignment of the prime focus corrector) and a 200 micron warp in the Tek 2k CCD. The latter means that it is impossible to focus the whole CCD, and because of the former, elliptical PSFs result. Fig. 4 shows the ellipticity and orientation for 193 stars in the combined  $B_J$ -band image of RXJ1347-1145. As expected the shape and orientation of the stars are correlated with position on the image. Since the distortion due to weak lensing is very small, this PSF anisotropy, if left uncorrected, will complicate the interpretation of the data.

For this paper we choose to correct for PSF anisotropy by devising a position-dependent convolution kernel which circularizes the PSF. After convolving the image with the kernel the PSFs should be substantially rounder and large scale correlations of shape and orientation will be removed. Unfortunately, a circularizing kernel will also blur the PSF somewhat, so we constrain the kernel to minimize this blurring effect. Additional constraints are that it be flux conserving and have all elements greater than or equal to zero.

The first step in constructing the kernel is to measure the usual quadratic moments for all the stars:

$$\begin{aligned}
 I_{xx}(PSF) &= \frac{\sum F_i x_i^2}{\sum F_i}, \\
 I_{yy}(PSF) &= \frac{\sum F_i y_i^2}{\sum F_i}, \\
 I_{xy}(PSF) &= \frac{\sum F_i x_i y_i}{\sum F_i},
 \end{aligned}
 \tag{1}$$

where  $F_i$  is the intensity of pixel  $i$  minus the sky background intensity. A kernel ( $K$ ) which satisfies our criteria and will circularize a PSF having  $I_{xx}(PSF)$ ,  $I_{yy}(PSF)$ , and  $I_{xy}(PSF)$  has:

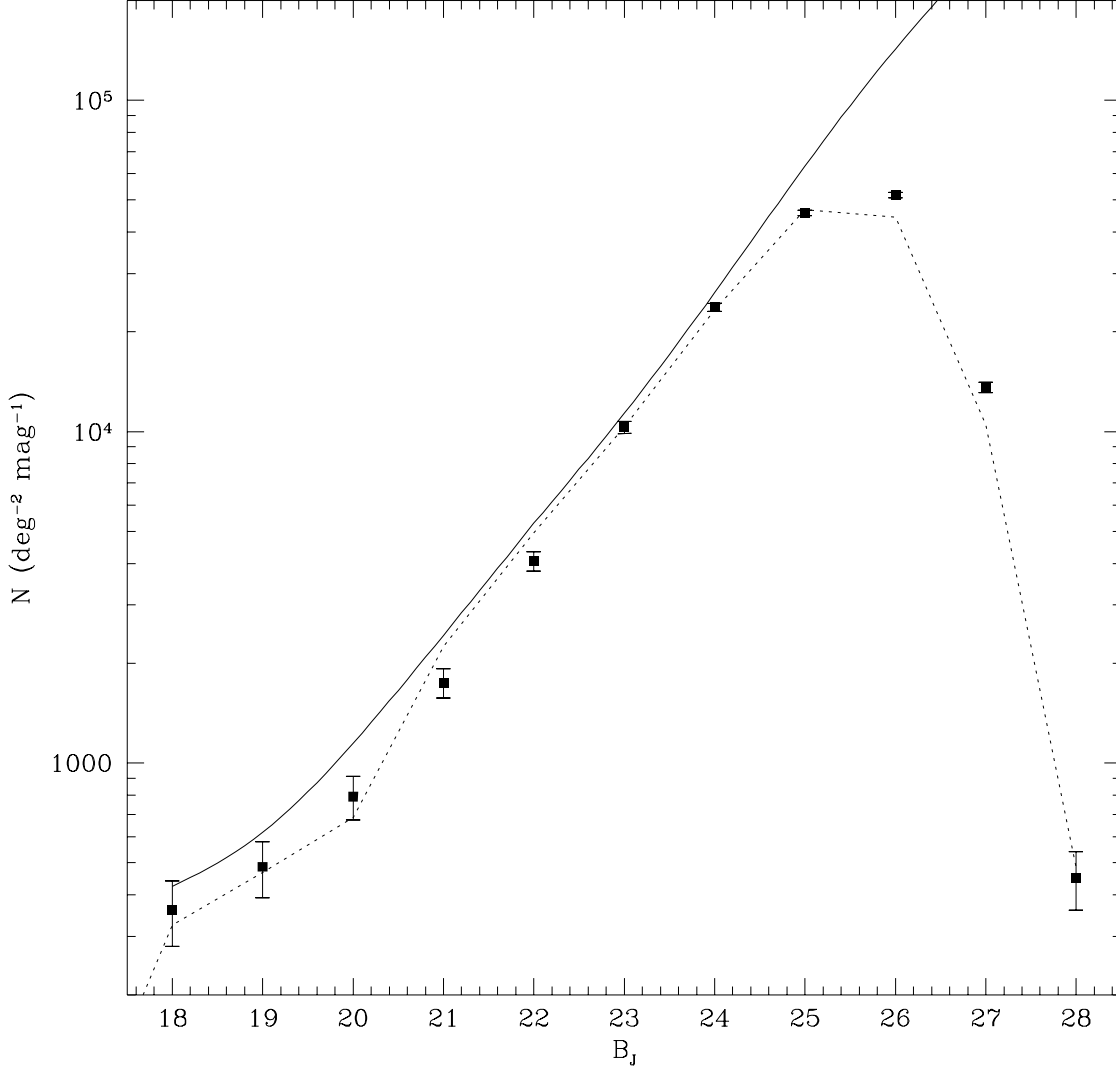


Fig. 2.— Counts for objects (stars and galaxies) detected in the field of RXJ 1347.5-1145. The points are the data, the solid line is the input model for the simulations and the dashed line is the result from one of the simulations. The magnitudes are the total magnitude within an outer isophote of 28.9  $B_J$  mag per square arcsecond

Fig. 3.—  $B_J$ - $R$  color-magnitude diagram of objects in the field around RXJ1347.5-1145. The  $B_J$  magnitudes are isophotal magnitudes (see Fig. 2) and the colors are derived in an aperture of 1.3'' radius. The lower panel is the whole field containing 5870 objects while the lower panel is the inner 90'' (303 objects).

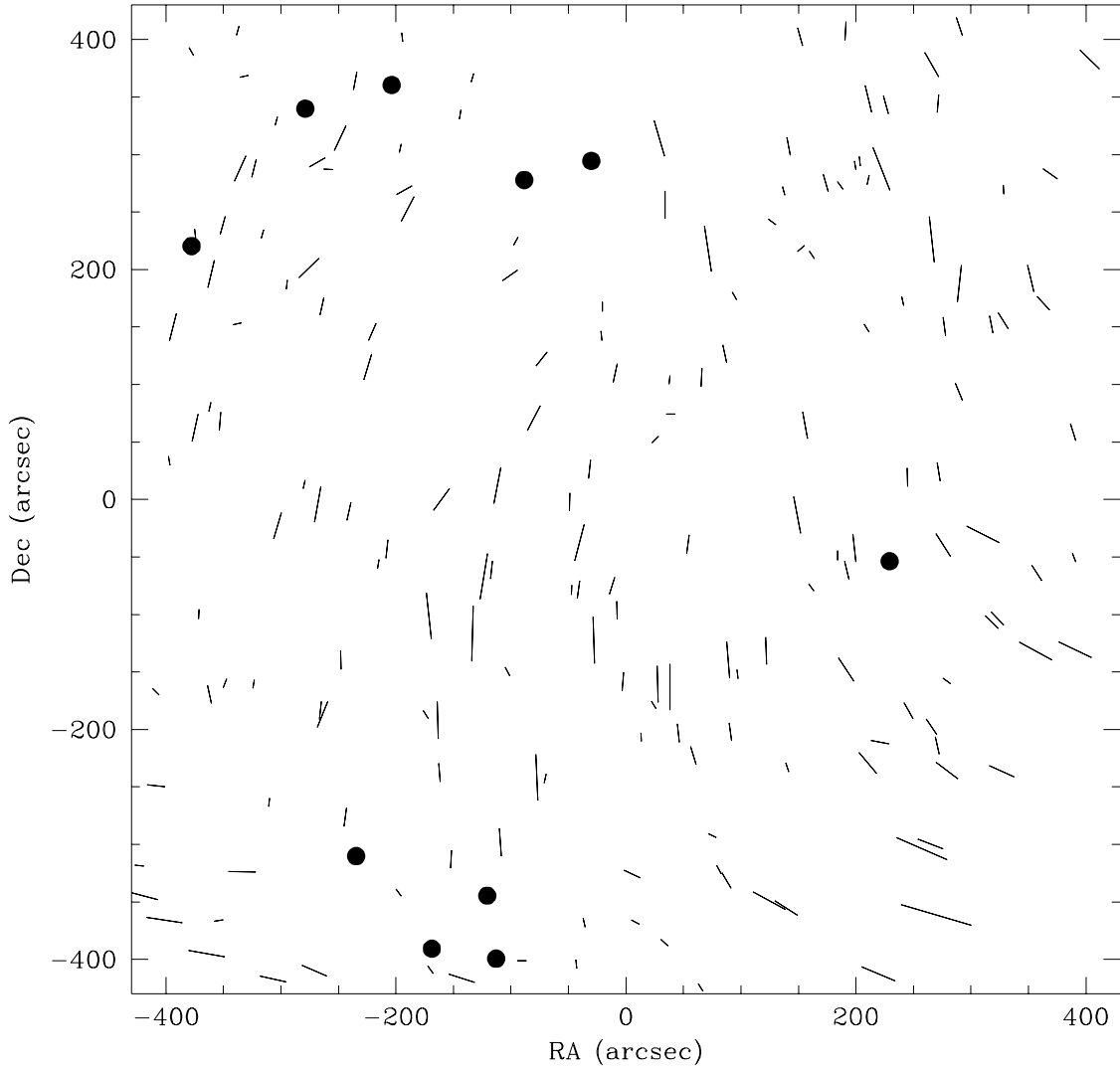


Fig. 4.— Ellipticity and orientation for 193 stars in the combined  $B_J$ -band image. Solid circles indicate stars which have  $\epsilon < 0.005$ . The maximum ellipticity is  $\epsilon = 0.08$  and the mean is  $\langle \epsilon \rangle = 0.02$ . The shapes and orientations of the stars are clearly correlated with position in this image. North is up and East is to the left.

$$\begin{aligned}
 I_{xx}(K) &= |I_{xy}(PSF)| \\
 I_{yy}(K) &= I_{xx}(PSF) - I_{yy}(PSF) + |I_{xy}(PSF)| \\
 I_{xy}(K) &= -I_{xy}(PSF)
 \end{aligned}
 \left. \vphantom{\begin{aligned} I_{xx}(K) \\ I_{yy}(K) \\ I_{xy}(K) \end{aligned}} \right\} I_{xx}(PSF) > I_{yy}(PSF)$$
  

$$\begin{aligned}
 I_{xx}(K) &= I_{yy}(PSF) - I_{xx}(PSF) + |I_{xy}(PSF)| \\
 I_{yy}(K) &= |I_{xy}(PSF)| \\
 I_{xy}(K) &= -I_{xy}(PSF)
 \end{aligned}
 \left. \vphantom{\begin{aligned} I_{xx}(K) \\ I_{yy}(K) \\ I_{xy}(K) \end{aligned}} \right\} I_{xx}(PSF) < I_{yy}(PSF)$$

(2)

The goal is to produce a kernel which, when convolved with the original image, will yield PSFs with  $I_{xx} = I_{yy}$  and  $I_{xy} = 0$ , within measurement error. The corresponding nine element convolution kernel which minimizes image blurring, is flux conserving, and positive everywhere has elements:

$$\begin{aligned}
 K(1,1) &= K(3,3) = 0.25[I_{xx}(K) + I_{yy}(K) + I_{xy}(K) - 1 + K(2,2)] \\
 K(1,2) &= K(3,2) = 0.5[1 - I_{yy}(K) - K(2,2)] \\
 K(2,2) &= \min[1 - I_{xx}(K), 1 - I_{yy}(K)] \\
 K(3,1) &= K(1,3) = 0.25[I_{xx}(K) + I_{yy}(K) - I_{xy}(K) - 1 + K(2,2)] \\
 K(2,3) &= K(2,1) = 0.5[1 - I_{xx}(K) - K(2,2)]
 \end{aligned}$$

(3)

As can be seen from 3 the elements of the kernel are only dependent on  $I_{xy}(PSF)$  and  $I_{xx}(PSF) - I_{yy}(PSF)$ . In order to correct the CCD image we fit third order polynomials to  $f_1(x, y) = [I_{xx}(PSF) - I_{yy}(PSF)]$  and  $f_2(x, y) = I_{xy}(PSF)$ . If we know the values of  $f_1$  and  $f_2$  everywhere on the image we can construct a position dependent kernel using the prescription given by 3. We then convolve our image with the kernel removing most of the PSF anisotropy. Fig. 5 shows the PSFs after the convolution; the mean measured ellipticity has been reduced from  $\langle \epsilon \rangle = 0.02$  to  $\langle \epsilon \rangle = 0.01$  and the shapes and orientation are no longer correlated with position. This is quantified further in §5 and §6.3.

## 5. Shear

For gravitational lensing, the relationship between the tangential shear,  $\gamma_T$ , and surface mass density,  $\Sigma$ , is (Miralda-Escudé 1991, 1995),

$$\gamma_T(r) = \bar{\kappa}(\leq r) - \bar{\kappa}(r),$$

(4)

where  $\kappa = \Sigma/\Sigma_{crit}$ , the ratio of the surface density to the critical surface density for multiple lensing, and  $r$  is the angular distance from a given point in the mass distribution. The critical density depends on the redshift distribution of the background galaxies. The first term on the right is the mean density interior to  $r$  and the second term is the mean density at  $r$ . Therefore, the presence of a foreground mass distribution will distort the appearance of background galaxies. For a given coordinate on the image ( $\vec{r}$ ), the distortion quantity for the  $i^{th}$  galaxy is:

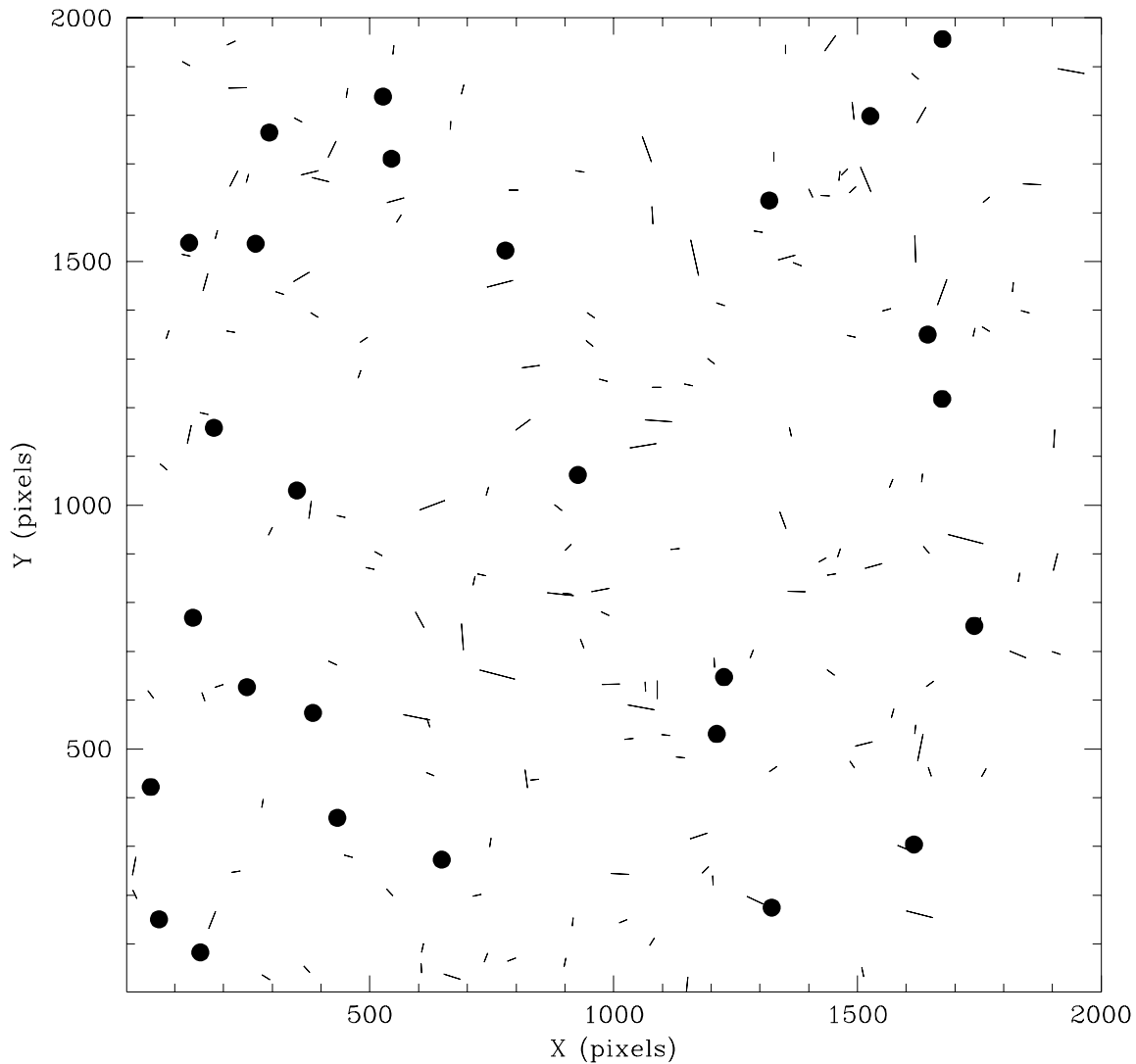


Fig. 5.— Ellipticity and orientation for the same 193 stars as in Fig. 4 after convolution with a position dependent kernel designed to circularize the PSF. Solid circles indicate stars which have  $\epsilon < 0.005$ . The maximum ellipticity is  $\epsilon = 0.04$  and the mean is  $\langle \epsilon \rangle = 0.01$ . The shape and orientation are no longer correlated with position.

$$D_i(\vec{r}) = \frac{1 - (b_i/a_i)^2}{1 + (b_i/a_i)^2} \times \frac{[\cos(2\theta_i)(\Delta x_i^2 - \Delta y_i^2) + 2 \sin(2\theta_i)\Delta x_i\Delta y_i]}{\Delta x_i^2 + \Delta y_i^2}, \quad (5)$$

where  $(b_i/a_i)$  and  $\theta_i$  are the galaxy axis ratio and position angle, respectively.  $\Delta x$  and  $\Delta y$  are the horizontal and vertical angular distances from  $\vec{r}$  to galaxy  $i$ . The value of  $D_i$  is a maximum when the position angle of the  $i^{th}$  galaxy major axis is perpendicular to the line joining  $\vec{r}$  to the galaxy and a minimum when it is parallel.  $D$  is related to the tangential shear by (Schneider & Seitz 1995):

$$\langle D(r) \rangle = 2 \frac{\gamma_T(r)[1 - \kappa(r)]}{[1 - \kappa(r)]^2 + \gamma_T^2(r)} \quad (6)$$

In the weak lensing regime  $\kappa \ll 1$ , and  $\gamma_T \ll 1$ ,  $\gamma_T \approx \langle D \rangle / 2$ .

The value of the mean distortion,  $\langle D(\vec{r}) \rangle$ , for  $\vec{r}$  equal to the position of the CDG in RXJ1347.5-1145 for 1970 galaxies in the combined  $B_J$  image having  $23.0 \leq B_J \leq 25.0$  in the radial range  $35'' \leq r \leq 400''$  is  $\langle D \rangle = 0.031 \pm 0.004$ ; the signal-to-noise is around 7.5. For comparison, the value of  $\langle D(\vec{r}) \rangle$  for  $\vec{r}$  at the CDG location for the 193 PSF stars in the corrected image is  $0.0017 \pm 0.0008$ , less than 6% of the measured shear value. The PSF-induced distortion on the galaxies is actually smaller than this since they are resolved objects. Therefore, the residual PSF anisotropy has little effect on our cluster mass estimate.

The measured value of  $\langle D \rangle$  is affected by seeing and the shear polarizability of the galaxies (see Kaiser et al. 1995). In order to calibrate this effect we carry out simulations using the F450W Hubble Deep Field Data (HDF) (Williams et al. 1996), using the techniques described in Kaiser et al. (1995). This involves stretching the HDF data by  $1 + \delta$ , convolving with the PSF and adding noise. The values of  $D_i$  are measured for each galaxy and compared to the unstretched values of  $D_i$ . The quantity of interest is the recovery factor,  $C = \delta / \langle \Delta D_i \rangle$ . Unfortunately the transformation between F450W and  $B_J$  is dependent on galaxy type and redshift. In order to match the two bandpasses as closely as possible and therefore sample similar galaxy populations we choose a 2.0 magnitude range in the HDF data which yields the same surface number density of galaxies as in the RXJ 1347-1145 field for the range  $23.0 \leq B_J \leq 25.0$ . The resulting F450W magnitude range is  $22.5 \leq F450W_{HDF} \leq 24.5$ . The value of the recovery factor is  $\langle C \rangle = 3.0 \pm 0.15$ . This correction does not take into account the presence of stars which will further dilute the signal, however, this will be minor for the magnitude range considered. The diluting effect of cluster galaxies is discussed in §6.4.

Fig. 6 shows corrected  $\langle D(\vec{r}) \rangle$  vs. projected radius for  $\vec{r}$  at the CDG position. Also shown are the input and measured values for 100 simulations of a lens with a singular isothermal mass distribution with velocity dispersion  $\sigma = 1460 \text{ km s}^{-1}$  (see §6.2). Because the cluster magnifies the background galaxies as

$$Mag(r) = \frac{1}{[1 - \kappa(r)]^2 - \gamma(r)^2}, \quad (7)$$

the apparent magnitude range which the background galaxies would have had in the absence of lensing is a function of projected radius from the cluster center (assuming a circular mass distribution). Since mean redshift depends on unlensed magnitude, the mean redshift and hence  $\Sigma_{crit}$  are also functions of projected radius. Fig. 7 shows how  $\Sigma_{crit}$  varies as a function of projected radius for an isothermal lens with  $\sigma = 1460 \text{ km s}^{-1}$ ,  $z = 0.45$ , and source galaxies with  $23.0 \leq B_J \leq 25.0$ , assuming the galaxy redshift distribution described in §6.2. The values



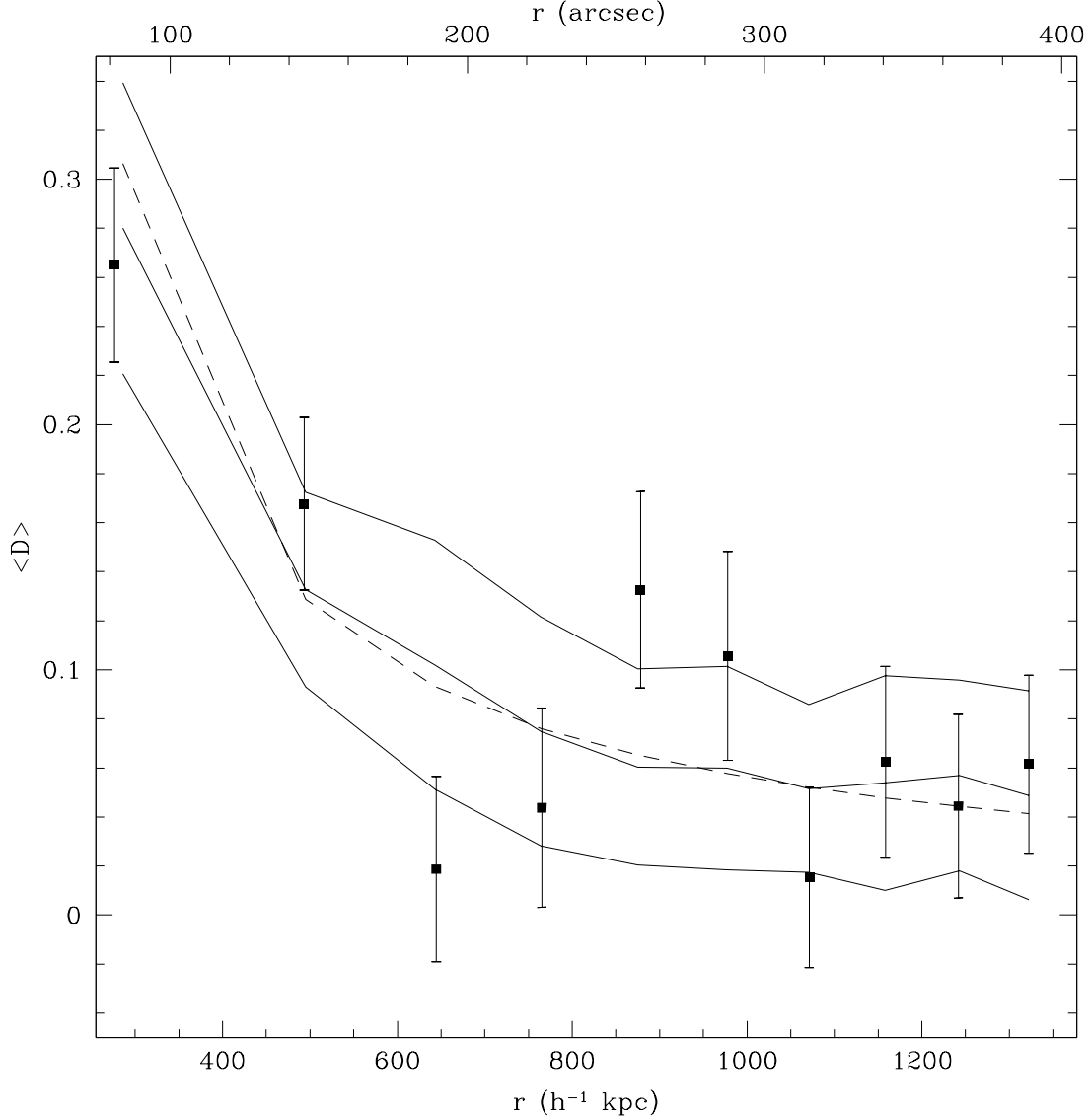


Fig. 6.— A plot of the distortion,  $\langle D \rangle$ , vs projected radius in radial bins containing 197 galaxies each ( $35'' \leq r \leq 400''$ ,  $23.0 \leq B_J \leq 25.0$ ), centered on the dominant cluster galaxy. The points are from the data ( $1\sigma$  error bars) and the solid lines are the mean and  $1\sigma$  upper and lower uncertainty bands from 100 Monte-Carlo simulations of a singular isothermal lens with  $\sigma = 1460 \text{ km s}^{-1}$ . These have been scaled by a recovery factor of  $C = 3.0$  (see text). The dashed line is the input model averaged over the radial bins and corrected for varying  $\Sigma_{crit}$ .

for  $\langle D \rangle$  for the isothermal model shown in Fig. 6 have been calculated assuming  $\Sigma_{crit}$  shown in Fig. 7 (the model used fits the lensing data well, see §6.4). Excellent agreement is seen between the input and measured  $\langle D \rangle$  values for the simulations, although the measured value is slightly below the input value for the innermost bin. The innermost bin is the most susceptible to systematic errors due to the strong lensing occurring in this bin and the large magnification factor.

The best value for the recovery factor from the simulations is  $C = 2.9 \pm 0.05$ , in agreement with the HDF simulations (although this agreement is expected since the simulated galaxy sizes were chosen such that they would yield the same recovery factor as the HDF simulations). The reduced  $\chi^2$  between the singular isothermal model and the data is  $\chi^2_\nu = 1.4$  ( $\nu = 9$ ). Because of the large uncertainties in the binned shear measurements it is not possible to put strong constraints on the shape of the mass profile.

## 6. Cluster Mass

### 6.1. Mass reconstruction

Formulae for 2-d mass reconstruction in the weak lensing regime have been discussed in Kaiser & Squires (1993) (KS) and Fahlman et al. (1994). Briefly, in the weak lensing regime, where  $\kappa \ll 1$ , the formula for the surface mass density is:

$$\kappa(\vec{r}) = \frac{1}{\bar{n}\pi} \sum_{i=1}^N \frac{W(\Delta x, \Delta y, s) D_i(\vec{r})}{\Delta x_i^2 + \Delta y_i^2}. \quad (8)$$

where  $N$  is the number of galaxies and  $\bar{n}$  is the number density of galaxies. Eqn. 8 assumes that the galaxies are intrinsically (in the absence of lensing) randomly aligned.  $W$  is a smoothing kernel which is required to prevent infinite formal error. In this paper we use a smoothing kernel of the form (Seitz & Schneider 1995):

$$W(\Delta x, \Delta y, s) = 1 - \left( 1 + \frac{\Delta x^2 + \Delta y^2}{2s^2} \right) e^{-(\Delta x^2 + \Delta y^2)/2s^2}, \quad (9)$$

where ‘ $s$ ’ is referred to as the “smoothing scale”. A 2-d mass map of RXJ 1347.5-1145 is shown in Fig. 8 and is discussed further in §6.3.

Because of the smoothing kernel, plus biases introduced by edge effects in the images, Eqn 8 is mainly useful for determining the 2-d shapes of mass distributions. A less biased way of obtaining mass estimates as well as azimuthally averaged density profiles is:

$$\bar{\kappa}(r \leq r_i) - \bar{\kappa}(r_i \leq r \leq r_o) = \frac{r_o^2}{N_{io}} \sum_{r_i \leq r \leq r_o} \frac{[1 - \kappa(\vec{r})][1 - \sqrt{1 - D_i(\vec{r})^2}]}{D_i(\vec{r})(\Delta x_i^2 + \Delta y_i^2)} \quad (10)$$

where  $N_{io}$  is the number of galaxies between  $r_i$  and  $r_o$ . This is similar to the form employed by Fahlman et al. (1994) but is valid when  $\kappa$  is not vanishingly small. Since  $\kappa$  appears on the right hand side of the equation, an iterative approach must be used to obtain the density profile. Radial mass profiles for RXJ1347.5-1145 are shown in Fig. 9 and are discussed further in §6.4.

It should be mentioned that galaxy distortion is insensitive to flat sheets of mass. Consequently, all mass measurements described in this paper are uncertain by an unknown additive constant. If there is a substantial flat component to the mass distribution our mass estimates will be lower limits. This is discussed further in §6.4.

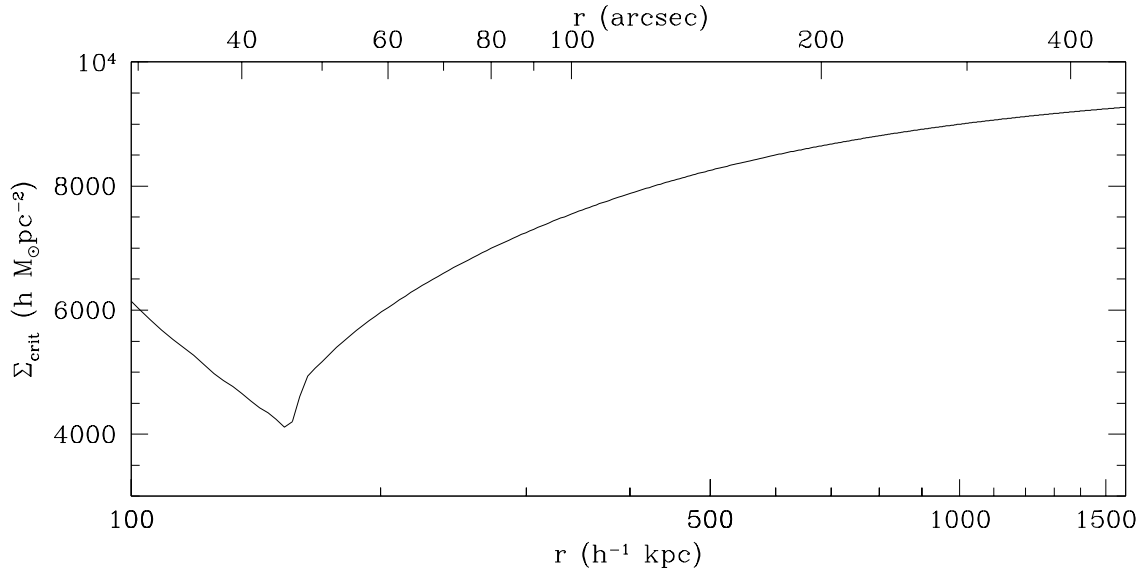


Fig. 7.—  $\Sigma_{crit}$  as a function of projected radius for an isothermal lens having  $\sigma = 1460 \text{ km s}^{-1}$ ,  $z = 0.45$ , and source galaxies with  $23.0 \leq B_J \leq 25.0$ .  $\Sigma_{crit}$  is dependent on radius because magnification by the cluster biases the source galaxy redshift upwards.

Fig. 8.— Mass map derived using Eqn. 8 with smoothing scale  $s = 43''$ . A total of 2735 galaxies with  $23.0 \leq B_J \leq 25.0$  are used in this reconstruction. The contours are spaced in  $1\sigma$  intervals. The peak of the mass distribution is consistent with the position of the central dominant galaxy. North is up and East is to the left. The field is  $14'$  on a side.

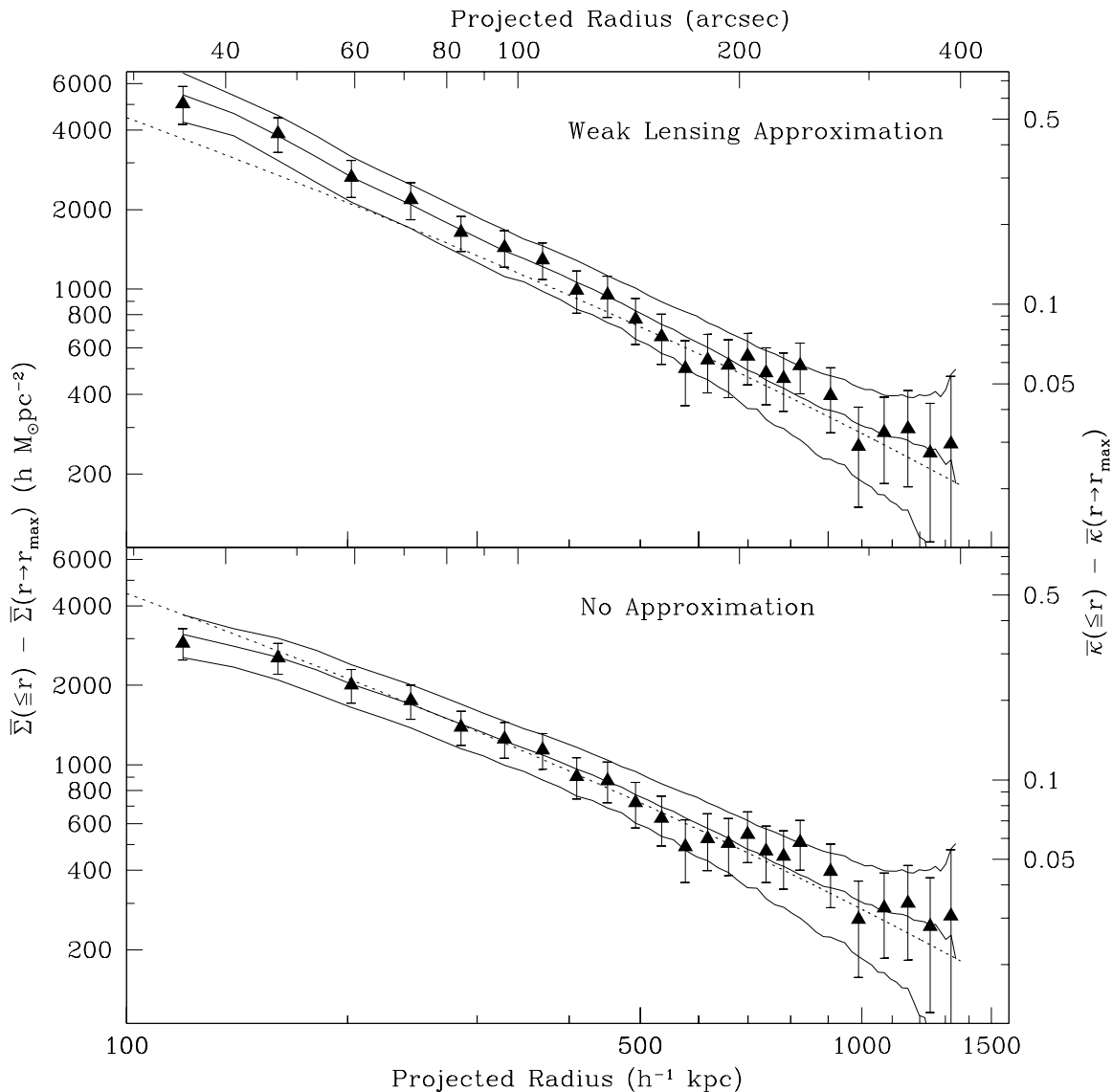


Fig. 9.— The upper panel is the radial mass density profile for RXJ 1347.4-1145 from Eqn. 10 assuming  $\kappa = 0$  and  $\Sigma_{crit}$  is a constant function of radius ( $r_{max} = 400'' = 1360h^{-1}$  kpc). It is centered on the central dominant galaxy. The points are the data for the cluster derived from 1970 galaxies having  $23.0 \leq B_J \leq 25.0$ . The solid line is the mean profile and the  $1\sigma$  upper and lower limits for 100 simulations of an isothermal spherical cluster having  $\sigma = 1460 \text{ km s}^{-1}$ . The input model is shown by the dotted line. The lower panel is the radial density profile from Eqn. 10 using  $\kappa$  derived from fits to the simulations and incorporating a radially varying  $\Sigma_{crit}$  as shown in Fig. 7. A recovery factor of  $C = 3.0$  (see text) has been applied.

## 6.2. Monte-Carlo Simulations

Before proceeding to a discussion of the mass reconstruction for the cluster we describe Monte-Carlo simulations of the data. These simulations are useful for identifying sources of systematic error which arise from seeing, measurement error and deviations from the weak lensing approximations, and for calibrating the data.

The simulations are discussed in detail in Fischer et al. (1996) and we briefly summarize them here. The simulations consist of artificial galaxies distributed in seven redshift shells ( $z = 0.0 - 0.45, 0.45 - 0.6, 0.6 - 0.7, 0.7 - 0.8, 0.8 - 1., 1.0 - 1.4, 1.4 - 7.0$ ). Galaxy images are generated for each shell based on the quiescent models of McLeod & Rieke (1995). Stars are also added to the simulated images based on the observed star counts. The size-absolute magnitude relationship for the simulated galaxies is adjusted to yield the same recovery factor as the HDF simulations and the simulated galaxies have a similar apparent ellipticity distribution to the observed galaxies. The galaxies in each shell are distorted with various spherically symmetric mass distributions located at  $z = 0.451$  under the assumption that all galaxies within a redshift shell lie at the number weighted mean redshift of that shell. Convolution with the PSF and the addition of noise are followed by identical processing to the real data. The results of the simulations will be discussed in the next section.

## 6.3. 2-d Mass Maps

The 2-d, KS mass map for RXJ1347.5-1145 is shown in Fig. 8 superposed on the R-band image of the field. This reconstruction used 2735 galaxies with  $23.0 \leq B_J \leq 25.0$ . The central peak has a signal-to-noise ratio of around 11 with  $s = 43''$ , and is consistent with the position of the CDG. The noise is calculated from maps derived from 100 simulations described above.

To check for biases introduced by residual anisotropies in the PSF, a similar map was produced using 193 stars detected in the field. The maximum in that map is 9% of the peak value in the cluster mass map (equal to the  $1.0\sigma$  noise level of the mass map) and the minimum is -6%. We conclude that residual PSF anisotropy is not significantly affecting the 2-d massmap. For comparison a map made from the same stars on the uncorrected image has a maximum of 17% of the mass map peak and minimum of -12%, and had large scale correlations not present in the corrected map.

The detectability of substructure in the mass map is limited by the surface density of background galaxies which is approximately  $13 \text{ arcmin}^{-2}$  in this case. The surface mass density contours appear to be fairly circular in the cluster central region and there are two  $3\sigma$  features in the southwest corner separated by about  $20'' = 70 h^{-1} \text{ kpc}$ . One worries about over-interpreting the KS mass map since the technique is known to produce spurious features (Schneider 1995). In order to test the significance of deviations from circularity in the KS mass reconstruction we have adopted the approach of Fischer et al. (1996). Ellipticity is computed from the quadrupole moments of the portions of the map with  $\kappa > 0$ . The upper panel of Fig. 10 shows this ellipticity value along with the distribution of ellipticities measured in an identical manner from the Monte-Carlo simulations, each of which contain spherical lenses. The RXJ 1347.5-1145 mass map is more elongated than 99 out of 100 simulations (Fig. 10). When we restrict the quadrupole moment calculation to  $r \leq 350''$  we find the cluster ellipticity falls within the range seen in the simulations. Therefore, the large ellipticity measured in the full field map is due to the subcluster in the southwest corner. We conclude that the subcluster is significant and unlikely to be an ar-

tifact of the KS image reconstruction. The subclumps are  $385''$  and  $500''$  from the cluster center ( $1.3$  and  $1.7 h^{-1}$  Mpc, respectively). Of course, the redshifts of the subclumps are unknown, and since the mass map is sensitive to mass over a large range of redshifts these subclumps may not be associated with the main cluster.

Fig. 11 is a contour plot of galaxy number density for galaxies in the range  $B_J \geq 20.45$  and  $B_J - R > 1.6$ . The center of the galaxy density map is consistent with the mass center and the position of the CDG. The galaxy map does not show evidence for subclustering in the southwest in this color range, however, both mass and galaxy maps do show evidence for extensions leading from the cluster center to the southeast.

#### 6.4. Mass Density Profile

In the upper panel of Fig. 9 we show the azimuthally averaged surface mass density profile centered on the CDG as derived from Eqn. 10 using 1970 galaxies having  $23.0 \leq B_J \leq 25.0$ . We have assumed that  $\kappa = 0$  on the right hand side and that the critical density is constant ( $\Sigma_{crit} = 9700h M_{\odot} \text{ pc}^{-2}$ ). Also shown is the mean measured mass profile for 100 simulations of a singular isothermal lens with  $\sigma = 1460 \text{ km s}^{-1}$  (see §6.2) which matches the radial profile for RXJ1347.5-1145 quite well. The measured simulated profile derived in this manner is much steeper than the input profile. However, if we now plug in the known values for  $\kappa$  (based on the input density profile and  $\Sigma_{crit}$  from Fig. 7) we get much better agreement between the input and derived density profiles for the simulations (bottom of Fig. 9). The innermost point is underestimated but this is the region where the magnification is the highest and the lensing effect is the strongest so we expect the largest systematic errors. Correcting the RXJ1347.5-1145 data in a similar way yields the points shown in the lower panel of Fig. 9. Therefore, the cluster profile appears to be consistent with a singular isothermal sphere having velocity dispersion  $\sigma = 1460 \pm 150 \text{ km s}^{-1}$ .

Note that the densities in Fig 9 are plotted as density contrasts; the mean density within a radius minus the mean density in a control annulus. The latter is estimated by extrapolating the density profile beyond the measured region so it is worth mentioning the relative values of the two. Based on the above mentioned singular isothermal model the control annuli densities vary from 8% of the total density for the innermost point to 50% for the outermost point.

The weak lensing signal will be diluted by cluster galaxies, and this dilution will be larger in the central regions. This will result in a systematic underestimate in the cluster mass, and will also flatten the inferred density profile. In order to estimate this effect we have looked at galaxies in the range  $23.0 \leq B_J \leq 25.0$  (the range used in the mass reconstruction) and compared the numbers of red galaxies having  $B_J - R \geq 1.6$  (see below) with the total number. We have assumed that the number density of the red galaxies at the edge of the field is dominated by field galaxies and have subtracted the mean density there ( $1.75 \text{ arcmin}^{-1}$ ) from the counts. We estimate that the sample of galaxies used to produce the innermost point in the radial density plot contains about 9% cluster galaxies declining to about 5% at large radius. These galaxies should be randomly aligned and therefore will have zero shear. If these galaxies have been included in the sum in Eqn. 10 then  $N_{io}$  will be overestimated and the density will be underestimated. Applying a correction for these cluster galaxies slightly steepens the density profile (although it is still consistent with the isothermal density profile) and increases the velocity dispersion to  $\sigma = 1500 \pm 160 \text{ km s}^{-1}$ .

In Fig. 12 we show the corrected surface mass density along with an isothermal profile having

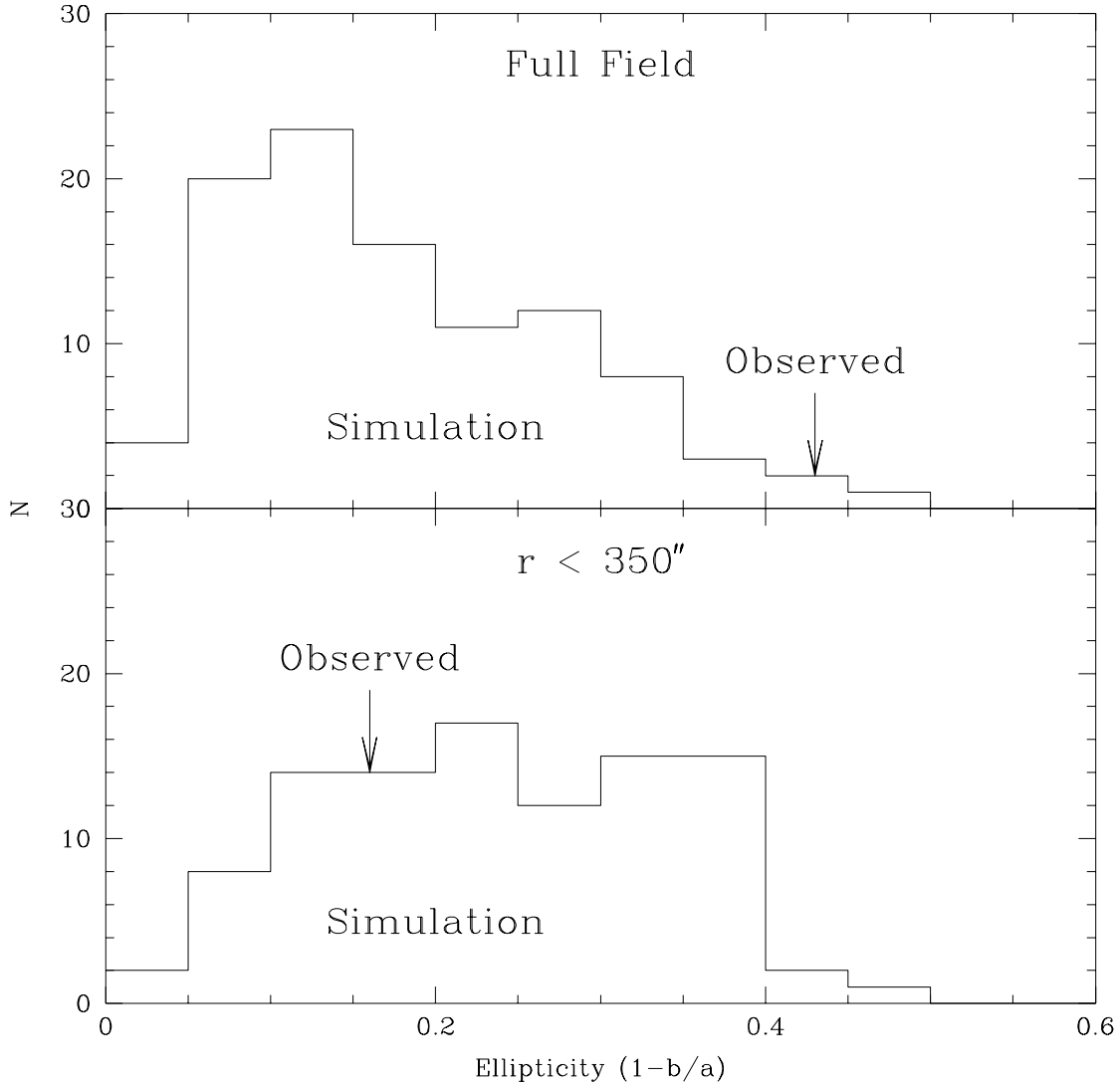


Fig. 10.— Histogram of ellipticity values for KS mass maps of 100 simulations of spherical isothermal lens ( $s = 43''$ ). The ellipticities are derived from quadrupole measurements of the positive portions of the mass maps. The upper panel shows the values for the full CCD field, the observed value for the RXJ1345.5-1145 field is indicated by the arrow. The cluster is more elongated than 99 out of 100 simulations. The lower panel shows the values for the region within  $350''$  of the CDG; the cluster falls within the range of the simulations in this region.

Fig. 11.— Number density contours of galaxies having  $B_J - R \geq 1.6$  superposed on the R band image of RXJ1347.5-1145. The contours are spaced by  $1\sigma$  ( $2.4 \text{ arcmin}^{-2}$ ) about the mean density ( $7.2 \text{ arcmin}^{-2}$ ). Orientation and size are as in Fig. 8

$\sigma = 1500 \text{ km s}^{-1}$ . Also plotted is the “universal” density profile of Navarro et al. (1995) which in 3-d is given by:

$$\frac{\rho(R)}{\bar{\rho}} = \frac{1500r_{200}^3}{R(5R + R_{200})}, \quad (11)$$

where  $\bar{\rho} = 2.78 \times 10^{-7}(1+z)^3 h^2 \text{ M}_\odot \text{ pc}^{-3}$  is the critical density of the universe and  $R_{200}$  is the radius for which the mean interior overdensity is 200. The curve shown in Fig. 12 for the surface density has  $R_{200} = 1.2h^{-1} \text{ Mpc}$  and is consistent with the data. In order to distinguish between these two density laws one would need data extending out to larger radius than we have here as the Navarro et al. surface density profile becomes steeper than an isothermal at large radius.

### 6.5. Mass-to-Light Ratio

Also in Fig. 12 we show the rest-frame B-band light contained in galaxies with  $R \geq 18.0$  for both  $B_J - R > 1.6$  and  $B_J - R > 0.0$ . There is little difference in the two light profiles, indicating that the cluster light is dominated by galaxies with observed  $B_J - R \geq 1.6$  (actually this only indicates that the radially varying component of the cluster light is dominated by red galaxies). We have only included light in galaxies out to an isophotal level of  $R = 29.8 \text{ mag}$  per square arcsec, any component more extended than this (for example a diffuse cluster component) is not included in the plotted luminosity profile or the mass-to-light ratio calculations described below.

The rest-frame B-band light is derived from the observed R-band light, requiring only a small correction, since, for  $z = 0.45$ , the central wavelength of the B bandpass (4490 Å) redshifts almost exactly to the center of R (6510 Å). There are two correction terms, the first due to redshift stretching of the bandpass and the second due to the relative calibration of the two bandpasses (based on the flux of A0 star). The absolute rest-frame B magnitude is given by:

$$M_B = R - 5 \log(D_l) + 5 - 2.5 \log(1+z) - 2.5 \log[f_R(A0)/f_B(A0)], \quad (12)$$

where  $D_l$  is the luminosity distance in  $h^{-1}$  parsecs, and  $f_R(A0)/f_B(A0)$  is the relative flux of an A0 star in the two bandpasses.

The luminosity density has been plotted as a density contrast similarly to the mass density. The mass and light profiles are consistent with one another for the entire radial range shown, with marginal evidence that the light profile is slightly steeper. They are also both consistent with a singular isothermal model. For  $r < 35''$  the luminosity density is steeper than isothermal (Not shown).

The implied rest-frame mass-to-light ratio is  $M/L_B = 200 \pm 50h \text{ M}_\odot/L_{B\odot}$  ( $M_{B\odot} = 5.48$ ). If we apply the estimated k-correction for early-type galaxies directly to the measured R-band light [ $k_{corr} = 0.625 \text{ mag}$  (Poggianti 1996)], we get  $M/L_R = 150 \pm 40h \text{ M}_\odot/L_{R\odot}$  ( $M_{R\odot} = 4.32$ ). According to Poggianti (1996) the estimated evolutionary correction for early type galaxies is  $B = -0.62 \text{ mag}$  for a  $z = 0.451$  galaxy, which agrees fairly well with the measured value for cluster ellipticals from Schade et al. (1997) of about  $0.47 \pm 0.15$ . Adopting these values and correcting to  $z = 0$  we get  $M/L_B = 310 - 350 \pm 90h \text{ M}_\odot/L_{B\odot}$ . Hughes (1989) found  $M/L_B = 280 - 360h \text{ M}_\odot/L_{B\odot}$  for the Coma cluster based on X-ray measurements and the assumption that mass traces light [in agreement with dynamical mass estimate of Colless & Dunn (1996)]. Therefore, RXJ1347.5-1145, despite being more than a factor of two more massive than Coma, appears to have a similar fraction of its mass in stars.



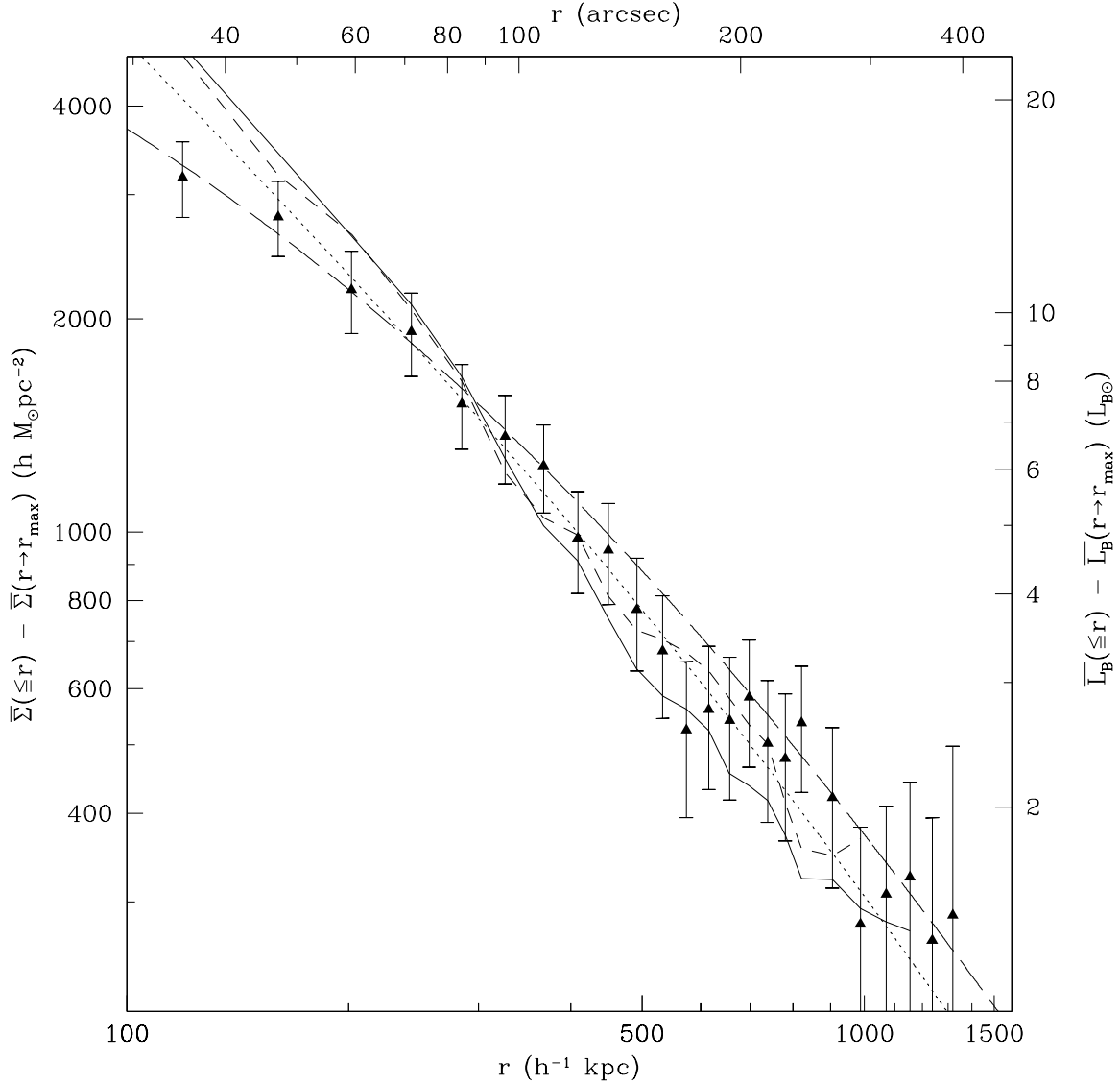


Fig. 12.— Plot of projected total cluster mass density and projected rest-frame B-band luminosity in galaxies. The luminosity density is shown for  $B_J \geq 20.45$  and  $B_J - R \geq 1.6$  (solid) and  $B_J - R \geq 0$  (short-dashed). The mass density is shown as points. Both densities are plotted as density contrasts. The dotted line is a singular isothermal model with  $\sigma = 1500 \text{ km s}^{-1}$  and the long-dashed line is the profile of Navarro et al (1995) with  $R_{200} = 1.2h^{-1} \text{ Mpc}$ . The mass and luminosity densities are consistent over the entire radial range plotted, with rest-frame  $M/L_B = 200 \pm 50h \text{ M}_\odot/L_{R\odot}$ . No significant difference is seen between the two different luminosity profiles indicating that the cluster light is dominated by galaxies with observed  $B_J - R \geq 1.6$ .

### 6.6. Arc Candidates

With an estimate of the mass density profile we can now predict the redshift of the two arc candidates, discovered by Schindler et al. (1995), under the assumption that they are strongly lensed background galaxies located at the Einstein radius. The arc candidates are located at projected distances of  $34.4''$  and  $36.0''$  from the CDG. The former has  $B_J = 23.0$  and  $B_J - R = 1.1$  while the latter has  $B_J = 21.9$  and  $B_J - R = 0.4$  and has a lower surface brightness; both are significantly bluer than the CDG. We estimate that, in order of distance from the cluster center, the arc redshifts are  $z = 1.4_{-0.35}^{+1.40}$  and  $z = 1.6_{-0.50}^{+2.00}$ , respectively. It should be mentioned that aside from being tangentially aligned to the center of the cluster, neither of these galaxies appears to be particularly arc-like (they are not highly elongated and no bending is apparent in our images) so the possibility remains that they are foreground field galaxies.

### 6.7. Comparison With X-ray Mass

There is a mass estimate for RXJ 1347.5-1145 based on X-ray data from both the ROSAT and ASCA satellites (Schindler et al 1996). This study used ROSAT HRI data to determine the shape of the radial profile and ASCA GIS data to measure the temperature. The cluster mass was estimated using the standard  $\beta$ -model technique (Cavaliere & Fusco-Femiano 1976), assuming hydrostatic equilibrium, spherical symmetry and isothermality, and was found to be  $M(R < 1h^{-1} \text{ Mpc}) = 5.8 \times 10^{14}h^{-1} M_{\odot}$  with a 15-20% quoted uncertainty. Our value from gravitational lensing is  $M(R < 1h^{-1} \text{ Mpc}) = 1.1 \pm 0.30 \times 10^{15}h^{-1} M_{\odot}$ , a factor of 1.8 higher than the X-ray mass estimate.

This mass difference is similar to what has been seen in comparisons between strong lensing and X-ray mass estimates at small projected radius for Abell 1689 and Abell 2218 (Miralda-Escude & Babul 1995), and between the weak-lensing and X-ray mass estimates of 0957+561 (Fischer et al. 1996). However, the weak lensing and X-ray masses for Abell 2218 are consistent out to  $0.4h^{-1} \text{ Mpc}$  (Squires et al. 1996a) and the same is true for Abell 2163 after the X-ray mass was used to estimate the mass density in the control annuli (Squires et al. 1996c).

The lensing mass estimate will be an overestimate if we have underestimated the mean redshift of the background galaxies. If we assume that all the background galaxies are at  $z = 3.0$ ,  $\Sigma_{crit}$ , and hence the inferred cluster mass, drops by about a factor of two (actually less than this since for part of our radial range we are assuming a lower  $\Sigma_{crit}$ , see Fig. 7). However, based on recent Keck redshift surveys, this is not possible. For example, Cowie et al. (1996) find a median redshift of around  $z \approx 0.8$  at  $B = 24.0$ , close to our adopted value for the range  $B_J = 23.0 - 25.0$ .

If one accepts the X-ray mass then one is led to the conclusion that this cluster is somewhat anomalous in several respects. The X-ray mass yields  $M/L_B = 110h M_{\odot}/L_{B\odot}$ , lower than seen in any other cluster. The value for  $M/L_X(\text{bol})$  [ $L_X(\text{bol}) = 2 \times 10^{46} \text{ erg s}^{-1}$ ] is much lower than is typically seen in other clusters (Sarazin 1988, Fig. 28), and the temperature (9.3 keV) is 35% lower than would have been expected for a cluster having the X-ray bolometric luminosity of RXJ 1347.5-1145 (David et al 1993). If the cluster temperature is underestimated one possible explanation is that it has been biased by an unresolved cooling flow. Schindler et al (1996) cite evidence for a large cooling flow, but due to the resolution limits of the ASCA data are not able to measure a central temperature decrement, and do not attempt to correct their temperature estimate. Finally, with the X-ray mass estimate, the gas mass fraction is very high, 34% within 1 Mpc and 52% within 3 Mpc ( $h = 0.5$ ). For the lensing mass estimate, the gas mass fraction is

reduced by a factor of 1.8, and falls within the range seen for other rich clusters within similar radii (White & Fabian 1995, Buote & Canizares 1996).

Currently there is considerable debate regarding the reliability of X-ray mass estimates. X-ray masses require the assumption of hydrostatic equilibrium, but cluster-cluster mergers can cause large deviations from this state. This in turn can lead to mass errors of  $> 100\%$  right after a merger and  $50\%$  for up to 2 Gyrs afterwards (Roettiger et al. 1996). Since predictions for typical cluster merger rates are approximately 1 every 2-4 Gyr (Edge et al. 1991) these sorts of X-ray mass errors are not unexpected for any given cluster measurement. Simulations following the formation of clusters in different cosmologies reveal a  $1\sigma$  scatter of  $30\%$  in cluster mass measurements based on the  $\beta$ -model (Evrard et al. 1996), indicating the uncertainties quoted by Schindler et al. (1996) are probably underestimated. Furthermore the presence of substructure generally results in X-ray masses which are underestimated if a spherical cluster is assumed. Finally, the difference in mass estimates could be reduced if the cluster is elongated along the line-of-sight, resulting in an underestimated X-ray mass.

## 7. Conclusion

In this paper we study the mass distribution of the  $z = 0.451$  X-ray cluster RXJ1347.5-1145 out to projected radii of  $1.4 h^{-1}$  Mpc by measuring the gravitationally-induced distortions of background galaxies. We detect a shear signal in the background galaxies in the radial range  $35'' \leq r \leq 400''$  significant at the  $7.5\sigma$  level. The resultant mass map exhibits an  $11\sigma$  peak centered on the dominant cluster galaxy. There is evidence for subclustering in mass at  $1.5 - 2.0 h^{-1}$  Mpc from the cluster center. However, since the weak lensing mass estimates are sensitive to mass over a large redshift range it is not certain that the subclusters are associated with the main cluster. No corresponding excess is detectable in the galaxy counts.

The azimuthally averaged mass and light profiles follow one another and are consistent with a singular isothermal model for the radial range  $120 \leq r \leq 1360 (h^{-1} \text{ kpc})$ . They are also consistent with the “universal” density profile of Navarro et al. (1995). The implied velocity dispersion (assuming isotropic distribution function) is  $\sigma = 1500 \pm 160 \text{ km s}^{-1}$ . The lensing mass estimate is almost two times higher than the recent X-ray mass estimate of Schindler et al. (1996). This large difference might be attributable to some combination of a recent merger, substructure, and elongation along the line-of-sight. The weak lensing mass estimate yields a rest-frame mass-to-light ratio of  $M/L_B = 200 \pm 50h M_{\odot}/L_{B\odot}$ . After estimated evolution correction this corresponds to  $M/L_B = 310 - 350 \pm 90h M_{\odot}/L_{B\odot}$  at  $z = 0$ , similar to what is seen in the Coma cluster, despite being over two times more massive.

Similar mass traces light behavior has been seen in other weak lensing studies (Tyson & Fischer 1995, Squires et al. 1996a, 1996b, 1996c) and in a radial velocity study of a sample of 16 clusters Carlberg et al (1996). These results argue against a significant velocity bias between the galaxies and the dark matter particles. Many simulations that follow the evolution of hierarchical galaxy formation in clusters show some degree of velocity bias (i.e. Carlberg 1994, Frenk et al. 1996). A direct comparison between the simulations and the cluster results is not straightforward due to the difficulty in identifying galaxies in the simulations. A further difficulty is that the simulations show the greatest velocity bias in the inner regions where the X-ray masses are the most in doubt and the lensing masses are incomplete. Therefore, it is probably fair to say that most simulations are not grossly inconsistent with the mass-traces-light result but any simulations which predict a large bias over the relevant radial ranges are suspect.

Support for this work was provided by NASA through grant # HF-01069.01-94A from the Space Telescope Science Institute, which is operated by the Association of Universities for Research in Astronomy Inc., under NASA contract NAS5-26555. Thanks to Gary Bernstein for assistance in devising the circularizing kernel and for reading an earlier draft of this paper. Thanks to Joe Mohr for interesting discussions/arguments. We also thank the referee, Gus Evrard for many helpful comments which improved the paper.

## REFERENCES

- Buote, D. A. & Canizares, C. R. 1996, *ApJ*, 457, 565.
- Cavaliere, A. & Fusco-Femiano, R. 1976, *A&A*, 49, 137.
- Colless, M. & Dunn, A. M. 1996, *ApJ*, 458, 435.
- Cowie, L. L., Songaila, A., Hu, E. M., Cohen, J. G. 1996, *ApJ*, 112, 839.
- Crone, M. M., Evrard, A. E., Richstone, D. O. 1994, *ApJ*, 434, 402.
- Crone, M. M., Evrard, A. E., Richstone, D. O. 1996, *ApJ*, 467, 489.
- David, L. P., Slyz, A., Jones, C., Forman, W., & Vrtilik, D. 1993, *ApJ*, 412, 479.
- Evrard, A. E., Metzler, C. A., & Navarro, J. F. 1996, *ApJ*, 469, 494.
- Evrard, A. E. 1997, astro-ph/9701148
- Fahlman, G.G., Kaiser, N., Squires, G. & Woods, D. 1994, *ApJ*, 436, 56.
- Fischer, P., Bernstein, G., Rhee, G. & Tyson, J. A. 1996, *AJ*, to appear in the Feb. 1996 *AJ*.
- Frenk, C. S., Evrard, A. E., White, S. D. M. & Summers, F. J. 1996, *ApJ*, 472, 460.
- Kaiser, N. & Squires, G. 1993, *ApJ*, 404, 441
- Kaiser, N., Squires, G. & Broadhurst, T. 1995, *ApJ*, 449, 460.
- Miralda-Escudé, J. 1995, in “IAU 173: Astrophysical Applications of Gravitational Lensing”, eds. C. S. Kochanek & J. N. Hewitt, (Kluwer), p. 131.
- Miralda-Escudé, J. & Babul, A. 1995, *ApJ*, 449, 18.
- Navarro, J. F., Frenk, C. S., & White, S. D. M. 1995, *MNRAS*, 275, 720.
- Poggianti, B. M. 1996, *A&A*, in press.
- Richstone, D. O., Loeb, A., & Turner, E. L. 1992, *ApJ*, 393, 477.
- Roettiger, K., Burns, J. O., & Loken, C. 1996, preprint.
- Sarazin, C. L. 1988, *X-ray Emissions from Clusters of Galaxies*, (Cambridge University Press).
- Schade, D. Barrientos, F., & Lopez-Cruz, O. 1997 *ApJ* 477, L???
- Schindler et al. 1995, *A&A*, 299, 9.
- Schindler, S., Hattori, M., Neumann, D. M., & Bohringer, H. 1996, preprint.
- Schneider, P. 1995, *A&A*, 302, 639.
- Seitz, C. & Schneider, P. 1995, *A&A*, 297, 287.
- Squires, G, Kaiser, N., Babul, A., Fahlman, G., Woods, D., Neumann, D., & Boehringer, H. 1996a, *ApJ*, 461, 572.

- Squires, G, Kaiser, N., Fahlman, G., Babul, A. & Woods, D. 1996b, *ApJ*, 469, 73.
- Squires, G, Kaiser, A., Fahlman, G., N., Babul, Woods, D., Neumann, D., & Boehringer, H. 1996c, preprint.
- Steidel, C. C, Giavalisco, M., Pettini, M., Dickinson, M., & Adelberger, K. L. 1996, *ApJ*, 462, 17.
- Tyson, J.A., Valdes, F. & Wenk, R.A. 1990, *ApJ*, 349, L1.
- Tyson, J. A. & Fischer, P. 1995, *ApJ*, L55.
- White, D. A., & Fabian, A. C. 1995, *MNRAS*, 273, 72.
- Wilson, G., Cole, S., & Frenk, C. S. 1996, *MNRAS*, 280, 199.
- Williams et al. 1996, *AJ*, 112, 1335.